scientific reports

Check for updates

OPEN

Elucidating refractive index sensitivity on subradiant, superradiant, and fano resonance modes in single palladium-coated gold nanorods

Metya Indah Firmanti[1] & Ji Won Ha[1,2]✉

Herein, we investigated the distinctive scattering properties exhibited by single gold nanorods coated with palladium (AuNRs@Pd), with variations in the Pd shell thicknesses and morphologies. AuNRs@Pd were synthesized through bottom-up epitaxial Pd growth using two different concentrations of Pd precursor. These single AuNRs@Pd displayed the characteristic of subradiant and superradiant localized surface plasmon resonance peaks, characterized by a noticeable gap marked by a Fano dip. We revealed the effect of local refractive index (RI) on the subradiant and superradiant peak energies, as well as the Fano dip in the scattering spectra of AuNRs@Pd with different Pd shell thicknesses. We demonstrated the applicability of the inflection points (IFs) method on detecting peaks and dip changes across different RIs. Thin AuNRs@Pd_{1mM} displayed more pronounced sensitivity to peak shifts in response to variations in local RIs compared to thick AuNRs@Pd_{2mM}. In contrast, thick AuNRs@Pd_{2mM} exhibited greater sensitivity to changes in curvature near the subradiant and superradiant peak energies rather than peak shift sensitivity across different local RIs. Moreover, the Fano dip shift was more noticeable in thick AuNRs@Pd_{2mM} compared to thin AuNRs@Pd_{1mM} across different local RIs. Therefore, we provided new insight into the RI sensitivity on subradiant, superradiant, and Fano resonance modes in single AuNRs@Pd.

Keywords AuNRs@Pd, Fano resonance, Inflection point, Localized surface plasmon resonance, Refractive index sensitivity

Plasmonic bimetallic nanoparticles have gained appreciable attention these days because of their versatile applications in nanoprobing and photocatalysis[1–5]. These types of nanostructures are often used owing to their distinctive properties, which combine the remarkable optical properties of plasmonic metal (Au, Ag, etc.) and electronic properties of catalytically-active metal (Pd, Pt, Ru, etc.)[6,7]. This enables the simultaneous utilization of thermal energy (photothermal effect) and photon flux (photoelectronic effect) from the plasmonic nanoparticle to the catalytic metal surface[8]. These dynamic effects can further be utilized to enhance the activity of catalytic metals. Due to this synergistic effect, the development of these bimetallic nanoparticles has grown vastly, including Au-Pt, Au–Pd, Au-Ni, Au-Fe, and Au-Cu[9–13].

Anisotropic gold nanorods (AuNRs), smaller than the wavelength of incident light, possess the ability to oscillate both transversally and longitudinally under the influence of photons driven by localized surface plasmon resonance (LSPR)[14]. The longitudinal LSPR mode typically resonates at lower energy levels and exhibits relatively higher intensity compared to the transversal LSPR mode, owing to the polarity induced on the longitudinal axis[15]. These electron cloud oscillations generate an electric dipole moment, facilitating hot-electron transfer from the higher Fermi level of Au to the lower Fermi level of the attached metals[16,17]. This entire process of hot-electron transfer, arising from contact electrification between plasmonic nanoparticles and metal featuring a more negatively charged Fermi level, is referred to as metal interface damping (MID), representing a component of the broad concept of surface plasmon damping[18]. Afterward, the hot electrons transferred from Au can increase the

[1]Department of Chemistry, University of Ulsan, 93 Daehak-ro, Nam-gu, Ulsan 44610, South Korea. [2]Energy Harvest-Storage Research Center (EHSRC), University of Ulsan, 93 Daehak-ro, Nam-gu, Ulsan, South Korea. ✉email: jwha77@ulsan.ac.kr

activity of catalytically active metals that have a more negative Fermi level than Au[19]. Pd, known for its unique electronic properties among other group 10 metals[16], holds numerous applications such as catalysts in hydrogenation as well as various C–C and C–heteroatom bonding reactions[20–23].

Unfortunately, there remains a lack of research on the fundamentals of the AuNR@Pd (core@shell) optical properties, particularly its sensitivity to refractive index (RI). Existing studies have shown the correlation between the LSPR peak of plasmonic nanoparticles and RI, with the LSPR peak typically red-shifting as RI increases[24–26]. Thus, comprehending the RI sensitivity of AuNRs@Pd is important for fine-tuning spectra and other optical properties, given the coupling between plasmonic scattering Au LSPR peak and the Pd scattering peak, such as Fano resonance resulting from the coupling of wide and narrow scattering peaks[18]. However, it is important to address the variability in RI due to its influence on the interactions between nanoparticles and light, as this may impact the catalytic effectiveness of bimetallic nanostructures when exposed to visible light. Furthermore, current research on these bimetallic nanoparticles predominantly emphasizes the electrochemical aspect to determine their photocatalytic ability, neglecting the spectrochemical aspect of the bimetallic nanostructures[4,27–29]. Hence, this study can serve as the initial investigation aimed at enhancing comprehension of the spectrochemical activity of AuNRs@Pd at the single-particle level. Therefore, an in-depth investigation into single-particle analysis on this subject would improve our understanding of the feasibility and tuning potential of using nanoparticles in a variety of photocatalysis applications[28–31].

Furthermore, research on the application of inflection points (IFs) method for multimodal scattering peak analysis remains limited. The IF method has emerged as a mathematical approach aimed at addressing the limitations of asymmetric peak broadening. This method has demonstrated its efficacy in enhancing the RI sensitivity. In numerous studies, higher RI sensitivities were observed at the IF points compared to the maximum LSPR peak in many Au nanoparticles[32–34]. Thus, this study also concentrated on assessing the feasibility of employing the IF method for analyzing spectra that exhibit multimodal peaks, particularly the LSPR scattering peak of AuNRs@Pd.

In this study, we investigated the characteristic scattering properties of a single AuNRs@Pd through dark-field (DF) microscopy and spectroscopy to eliminate the ensemble averaging of nanoparticles. We then demonstrated the effect of the surrounding medium on the RI sensitivity of single AuNRs@Pd across its subradiant, superradiant, and Fano resonance modes. This was achieved by analyzing the scattering peak of single nanoparticles using the IF method in three different media.

Results and discussion

AuNRs@Pd were synthesized via bottom-up epitaxial Pd growth, incorporating Pd precursor (H_2PdCl_4), reducing agent (ascorbic acid, AA), surfactant (cetyltrimethylammonium bromide, CTAB), and hydrochloric acid (HCl) into the AuNR solution[18,35]. In this study, two different Pd concentrations of 1 and 2 mM were used to synthesize AuNRs@Pd with different shell thicknesses and morphologies. Structural characterizations of the nanoparticles were conducted using scanning electron microscopy (SEM) and transmission electron microscopy (TEM). Figures 1A and S1 depict SEM images of CTAB-capped AuNRs with an average size of 72.31 (± 7.254) nm × 25.90 (± 2.276) nm (Fig. S2). The thick AuNRs@Pd_{2mM}, synthesized using 2 mM of Pd precursor, showed coarse and bumpy shell structures, as shown in the high-resolution TEM (HR-TEM) results (Figs. 1B and S3). The formation of the thick Pd shell on AuNRs@Pd_{2mM} formed through layer-by-layer epitaxial growth before encountering tensile strain owing to lattice mismatch between Pd and Au lattices[18]. Consequently, Pd islands emerged to alleviate the stress caused by tensile strain on the Pd lattice. The thickness of the Pd islands extending from the core to the tip of thick AuNRs@Pd_{2mM} varied between 3.164 and 5.763 nm. Decreasing the Pd precursor concentration to 1 mM endorsed the formation of thin AuNRs@Pd_{1mM} with a smoother Pd shell (Figs. 1C and S4). SEM results revealed that the mean aspect ratio (AR) of thick AuNRs@Pd_{2mM} was determined at 2.47 (± 0.341) (Fig. 1D). However, the AR of thin AuNRs@Pd_{1mM} was 2.67 (± 0.354) exhibited greater value than that of thick AuNRs@Pd_{2mM} (Fig. 1D). This difference in AR was attributed to the thickness of the Pd shell, which influenced the dimensions of the bimetallic nanoparticles in terms of length and width.

We examined the distribution of Au and Pd on AuNRs@Pd_{2mM} using HR-TEM coupled with energy-dispersive X-ray spectroscopy (EDX). The elemental mapping images obtained from EDX revealed the presence of Pd islands on the AuNR surface, with Au and Pd distributed across the bimetallic nanoparticle (Fig. 2). Furthermore, Pd exhibited a preference for growth on Au (001) and Au (111) facets before reaching another lattice and undergoing reduction[36]. This observation aligns with the elemental mapping results of thick AuNR@Pd_{2mM}, indicating a higher concentration of Pd at the tip, as depicted in Fig. 2.

Subsequently, we investigated the scattering properties of the synthesized AuNRs@Pd using single-particle DF microscopy and spectroscopy to eliminate the ensemble averaging of nanoparticles. Figure 3A displays the DF scattering image of single thin AuNRs@Pd_{1mM}, with the corresponding scattering spectra, denoted by circles in Fig. 3A, presented in Fig. 3B. Meanwhile, Fig. 3C depicts the DF scattering image of a single thick AuNR@Pd_{2mM}, while the DF scattering spectra of representative single particles are shown in Fig. 3D. In complex plasmonic bimetallic nanostructures, the plasmonic resonance could be classified as the superradiant mode due to its strong coherence with incident light. Conversely, the subradiant mode in the spectra of this bimetallic nanostructure corresponded to the peak in the higher energy spectral range[37]. The superradiant peak was visible at low energy area. Additionally, a Fano dip was observed between the two peaks of the AuNRs@Pd scattering spectra, which arose from the overlapping peak between the narrow LSPR peak of Au and the wide scattering peak of Pd[18,38]. In the scattering spectra of thin AuNRs@Pd_{1mM}, we observed a tendency for the superradiant peak intensity to be higher compared to the subradiant peak intensity (Fig. 3B). Conversely, thick AuNR@Pd_{2mM} exhibited a higher intensity at its subradiant mode (Fig. 3D). The thicker Pd shell attenuated the characteristic of Au LSPR spectra, leading to a lower intensity of the superradiant scattering peak. Therefore, the thickness of the Pd shell is proven to influence the shape of scattering spectra of the bimetallic AuNRs@Pd. Besides the observed intensity

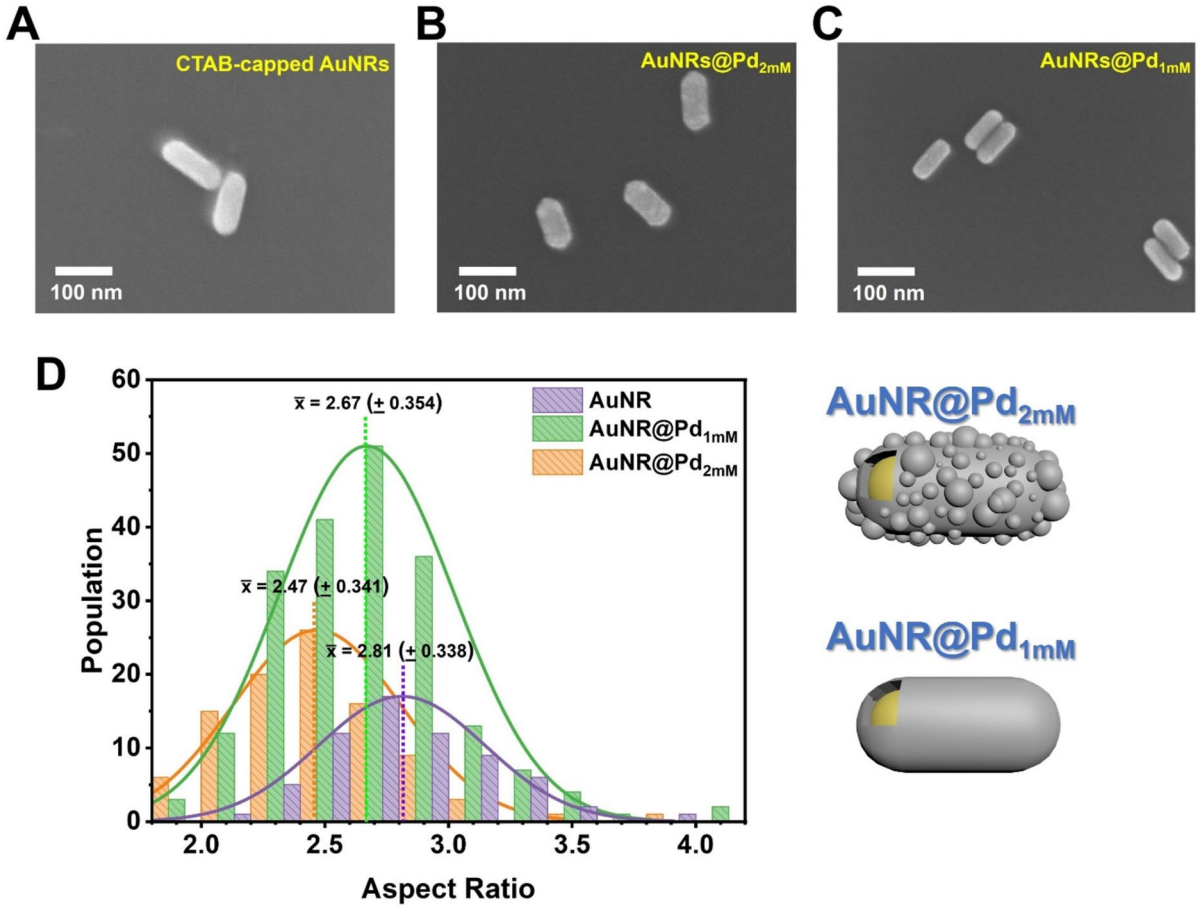

Fig. 1. (**A**) SEM image of CTAB-capped AuNRs utilized for the synthesis of AuNRs@Pd. (**B**) SEM image of thick AuNRs@Pd_{2mM} exhibits bimetallic nanoparticle structure with a bumpy surface. (**C**) SEM image of thin AuNRs@Pd_{1mM} depicts a notably smooth formation of the Pd shell on the surface. (**D**) The normal distributions of AuNR (purple), thin AuNRs@Pd_{1mM} (green), and thick AuNRs@Pd_{2mM} (orange) aspect ratios (AR) reveal the decrement in AR as the Pd concentration used increases.

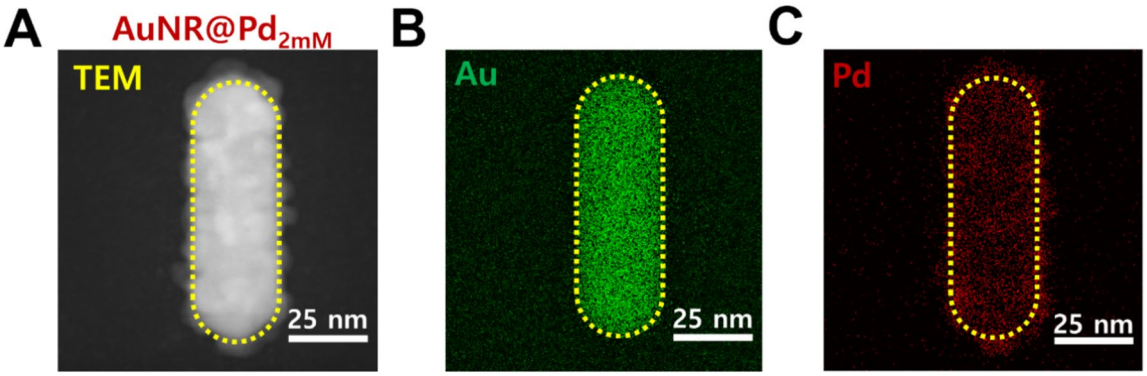

Fig. 2. (**A**–**C**) TEM–EDX results of thick AuNRs@Pd_{2mM}, revealing Pd deposition along the AuNR surface, with a preference for Pd deposition at the tip region, as evidenced through the elemental mapping of Pd (highlighted in red in **C**).

reduction in the Au spectra, the introduction of the Pd shell appeared to have a noticeable effect on the scattering intensity of the nanoparticle observed through DF microscopy. As illustrated in Fig. 3A and C, the DF image of AuNRs@Pd_{1mM} with high Pd contents on the shell, proven by a pronounced subradiant peak in its DF scattering spectra, exhibits a significant decrease in scattering intensity observed through DF microscopy (Fig. 3B and D).

The appearance of the subradiant and the superradiant peaks in the scattering spectra of AuNRs@Pd induced the existence of the Fano resonance, depicted as a dip. While multiple factors might contribute to the occurrence

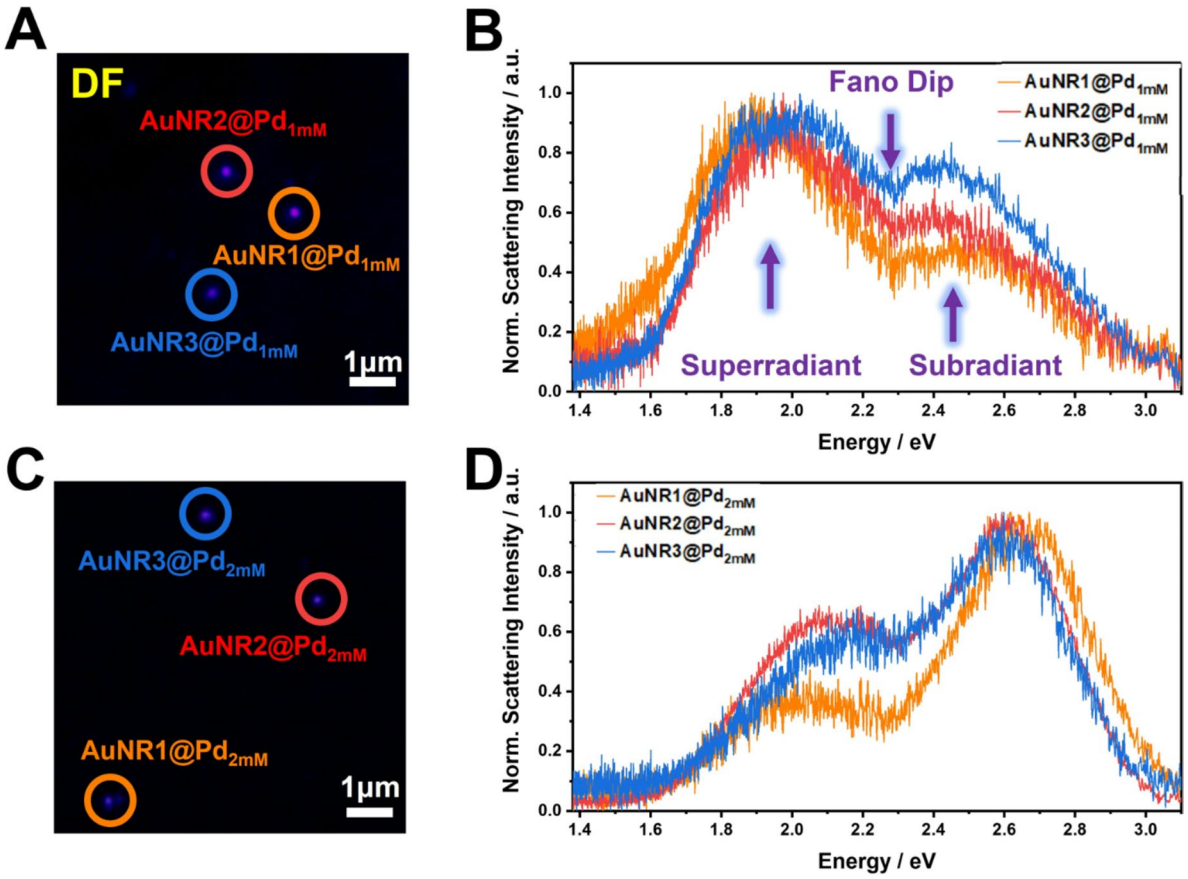

Fig. 3. (**A**) DF scattering image and (**B**) LSPR scattering spectra of thin Pd shell AuNRs@Pd_{1mM} exhibit the presence of two distinct peaks, namely superradiant (low energy) and subradiant (high energy), separated by the Fano dip. (**C**) DF scattering image and (**D**) LSPR scattering spectra of thick Pd shell AuNRs@Pd_{2mM} demonstrate higher intensity of the superradiant peak compared to its subradiant peak intensity.

of the Fano resonance, the overlap between two peaks, the broad Pd peak and the narrow Au LSPR peak, was the cause of the Fano resonance in the single-particle scattering spectra of AuNRs@Pd. Based on the results, the Fano energy of thick AuNR@Pd_{2mM} in a water medium was smaller than that of thin AuNRs@Pd_{1mM}, which were 2.2969 (± 0.0277) and 2.3142(± 0.0316) eV, respectively. Consistent with our previous findings, an increase in the concentration of Pd on the surface induced a blueshift of the superradiant peak[18]. The coupling between the Au and Pd peaks induced a phenomenon in which the superradiant peak, primarily associated with the Au resonance, underwent a shift towards higher energy level. Numerous prior investigations have confirmed the presence of the broad Pd peak within the wavelength range of 345–441 nm (equivalent to 2.81–3.59 eV), while the energy values of the Pd peak are typically higher than those of the Au LSPR peak (approximately 1–2 eV)[39–43]. Consequently, the reduced energy difference between the two peaks ($E_{Au} - E_{Pd}$) led to the appearance of a Fano dip (E_{Fano}) at lower energy levels when additional Pd was introduced to the surface of AuNR, as indicated using Eq. (1)[18]:

$$E_{Fano} \propto \frac{\left(q\Gamma_{Pd} + E_{Au} - E_{Pd}\right)^2}{\left(E_{Au} - E_{Pd}\right)^2 + \Gamma_{Pd}^2} \tag{1}$$

In Eq. (1), q denotes the Fano parameter, and Γ_{Pd} describes the linewidth of the continuous mode, which in this case the Pd scattering peak. The optimal value of q was determined by assessing the normalized Fano cross-section, calculated using Eq. (2). In this expression, ε represents the reduced energy, which is derived by dividing the difference between the Pd peak and the Fano resonance energy by the linewidth of Pd peak[18,44].

$$\sigma_{Fano} = \frac{\left(q + \varepsilon\right)^2}{\left(q^2 + 1\right)\left(\varepsilon^2 + 1\right)} \tag{2}$$

The results revealed a distinctive dip at lower energy compared to the peak energy of Pd, as reported in numerous prior studies ($E - E_{Pd} < 0$)[39–43]. Consequently, the ε value aligns with the observed trend of AuNRs@Pd scattering spectra when the q value is within the range of $0 < q < 1$[18].

We then investigated the effect of RI of the surrounding medium on subradiant, superradiant, and Fano resonance modes in single AuNRs@Pd. This study on the RI effect was conducted using air (RI = 1.000), water (RI = 1.333), and oil (RI = 1.518) as the surrounding medium (Figs. S5–S10). Scattering peak analysis was conducted using the IF method to determine the peak scattering energy of both peaks and the curvatures of the constructing peaks (subradiant and superradiant peaks). This mathematical approach was conducted by deriving the spectra curve of the bimetallic nanoparticle scattering spectra to obtain their first and second-order derivation curves. The first-order derivative IF points are located where the curvatures change sign, indicating the subradiant and superradiant peaks, as well as the Fano dip. Additional IF points are located where the concavity of the spectra changes sign, indicating changes in the slope of the constructing peaks, occurring when the second derivative of intensity with respect to wavelength or photon energy equals zero. Prior to calculation, the scattering peaks were smoothed using Savitzky–Golay (SG) smoothing to improve the signal-to-noise ratio[18,45]. This method was chosen for its underlying principle, which utilizes a locally-fitting data approach using polynomials through the method of least squares. This smoothing approach facilitates the smoothing of the scattering peak while preserving the shape of the single-particle scattering spectra[45]. The first, second, and third rows in Fig. 4A–C depict the scattering spectra of single AuNRs@Pd_{1mM}, along with their respective first and second-order derivatives in different media. The maxima of the superradiant plasmon scattering peak of AuNRs@Pd_{1mM}, denoted as IF B, were located at 1.982 (± 0.065), 1.967 (± 0.052), and 1.930 (± 0.032) eV in air, water, and oil, respectively. Meanwhile, the maxima of the subradiant plasmon scattering peak of AuNRs@Pd_{1mM}, indicated as IF F, were located at 2.461 (± 0.038), 2.444 (± 0.0415), and 2.425 (± 0.0783) eV for air, water, and oil, respectively. These results demonstrate the redshift of the peaks alongside the increment of the local dielectric constant, aligning with previous reports[18,46,47]. The Fano dip, represented by IF D, was located at 2.291 (± 0.021), 2.292 (± 0.025), and 2.326 (± 0.099) eV for air, water, and oil, respectively. These results confirm that the blueshift of the Fano dip on AuNRs@Pd is associated with the increase in RI. IF A and IF C represent the *x*-intercepts of the second derivatives of AuNR@Pd_{1mM} scattering spectra within the superradiant plasmon peak regime. The LSPR IF values of A and C were 1.797 (± 0.044) and 2.123 (± 0.064); 1.784 (± 0.041) and 2.101 (± 0.049); and 1.744 (± 0.034) and 2.078 (± 0.031) eV in air, water, and oil, respectively, ordered from lowest to highest RI. These findings illustrate the redshift of the inflection peaks value along with the increment of the local dielectric constant, similar with numerous previous reports[33,46,48]. Meanwhile, IF E and IF G describe the points where the second derivative of the scattering peak crosses the *x*-axis on the subradiant scattering peak regime of AuNR@Pd_{1mM}. The observation on IF E indicated a blueshift coinciding with an increase in the dielectric constant, contrary to the tendencies observed at other second-order derivation IFs, which were 2.379 (± 0.028); 2.395 (± 0.061); and

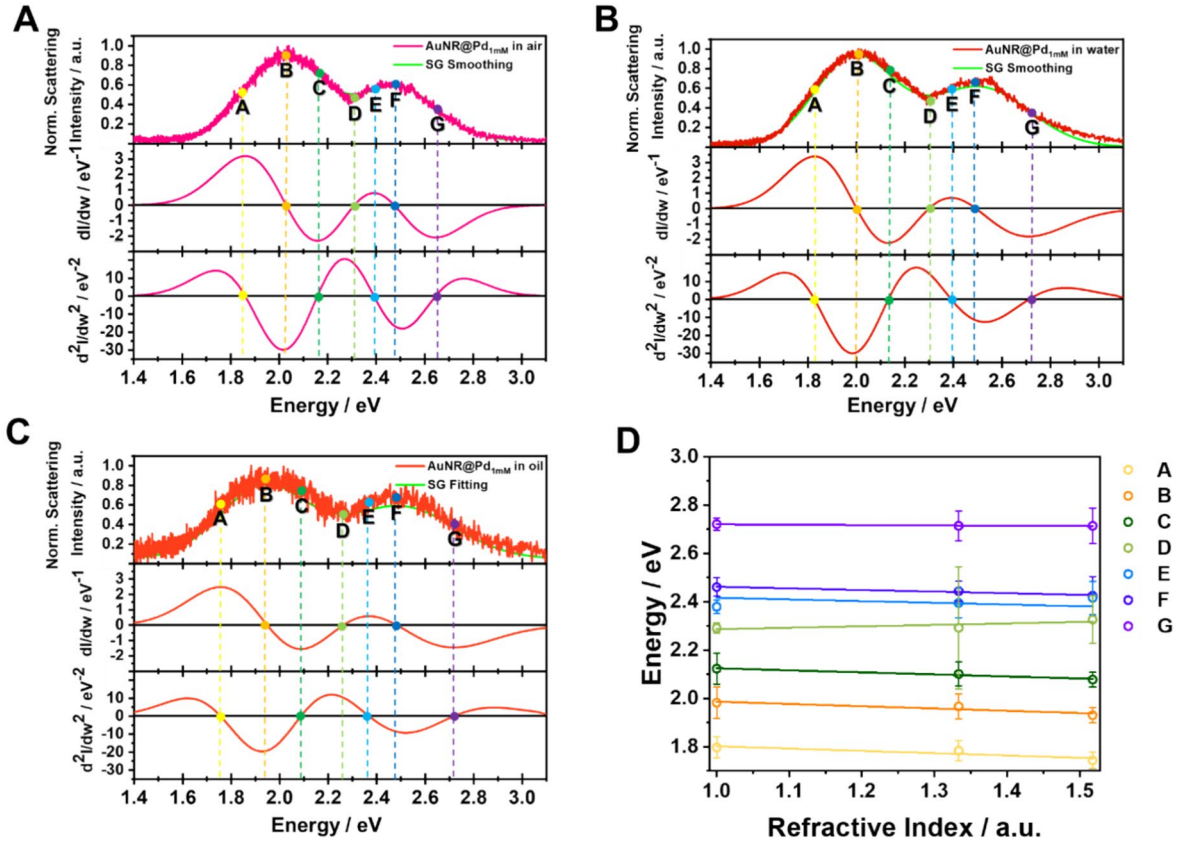

Fig. 4. (**A**–**C**) Inflection point method applied to the single-particle scattering spectra of thin AuNR@Pd_{1mM} across three different local RIs (air, water, and oil) (first row), along with its first (second row) and second (third row)-order derivatives. (**D**) Resulting inflection points plotted against the three local RIs for points A–G.

2.416 (± 0.069) eV in air, water, and oil, respectively, ordered from the lowest to the highest RI. In thin AuNRs@Pd_{1mM}, IF E describes the change in concavity of the subradiant peak close to the dip region, which has relatively low intensity compared to its superradiant peak. Therefore, the observed blueshift in IF E was predominantly caused by the coupling between the superradiant and subradiant peaks. Concurrently, the IF G demonstrated less noticeable shifts compared to any other IFs across different RI environments (Fig. 4D).

To further investigate the influence of the Pd shell thickness on single AuNRs@Pd scattering peak across different dielectric constant conditions, DF microscopy was performed on single thick AuNRs@Pd_{2mM} using similar medium variants. In this context, a high proportion of Pd will significantly dampen the superradiant plasmon peak scattering intensity of the bimetallic nanoparticles, identified as the plasmonic peak of Au, causing a shift to a lower wavelength (blueshift)[49]. Additionally, the epitaxial growth of the Pd shell beyond its critical thickness leads to the formation of islands, resulting in a bumpy Pd shell on the Au core surface[50]. The surface evolution of the bimetallic nanoparticles results in the weakening and blueshift of the plasmon resonance peaks[18,50]. Consequently, the scattering peaks of AuNRs@Pd_{2mM} exhibit a more pronounced blueshift compared to AuNR@Pd_{1mM}, as shown in IF B, which corresponds to the superradiant peak energy, and IF F, which corresponds to the subradiant peak energy of the bimetallic nanoparticle scattering spectra (Figs. 4D and 5D).

The first, second, and third rows in Fig. 5A–C depict the scattering spectra of single AuNRs@Pd_{2mM}, along with their respective first and second-order derivatives in different media. The maxima of the superradiant plasmon scattering peak of AuNRs@Pd_{2mM} indicated as IF B were located at 2.056 (± 0.053), 2.046 (± 0.053), and 2.035 (± 0.067) eV for air, water, and oil, respectively. Compared to AuNRs@Pd_{1mM}, the sensitivity of IF B of AuNRs@Pd_{2mM} toward RI changes was less pronounced owing to the attenuation of Au plasmon scattering peak (Fig. 5D). The damping of the Au core plasmon and the increase in scattering peak of the AuNRs@Pd subradiant peak upon light irradiation were attributed to the thicker Pd shell coating on the surface of Au core[27]. However, changes in the concavity of the thick AuNRs@Pd_{2mM} in the superradiant regime with respect to RI changes were more visible compared to its peak shift, as evidenced by the IF A results with values of 1.842 (± 0.039), 1.826 (± 0.044), and 1.815(± 0.053) eV in air, water, and oil, respectively, ordered from smallest to highest. The sensitivity of IF A was 1.27 times higher compared to IF B, with values of 51.345 (± 2.768) meV.RIU^{-1} ($R^2 = 0.9971$) and 40.41 (± 9.130) meV.RIU^{-1} ($R^2 = 0.9514$), respectively (Fig. 6). The coupling effect between superradiant and subradiant peaks in AuNRs@Pd_{2mM} scattering spectra led to a shift of the IF C towards higher energy levels along with the increment of RI. The peaks for subradiant plasmon peak of thick AuNRs@Pd_{2mM}, denoted as IF F, showed less sensitivity compared to thin AuNRs@Pd_{1mM}, with values located at 2.619 (± 0.013), 2.615 (± 0.019), and 2.587 (± 0.024) eV for air, water, and oil, respectively (Fig. 6). Aligned with the superradiant peak results, its

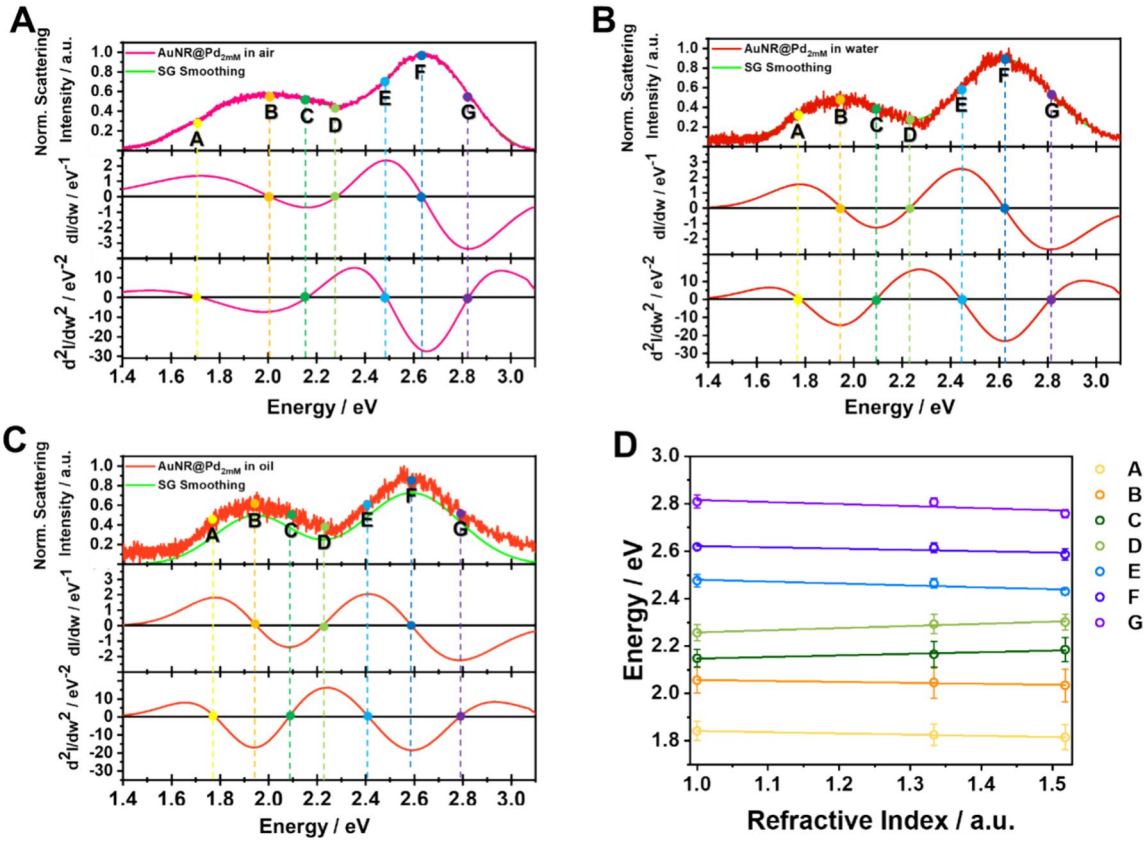

Fig. 5. (**A**–**C**) Inflection point method applied to the single-particle scattering spectra of thick AuNR@Pd_{2mM} across three different local RIs (air, water, and oil) (first row), along with its first (second row) and second (third row)-order derivatives. (**D**) Resulting inflection points plotted against the three local RIs for points A–G.

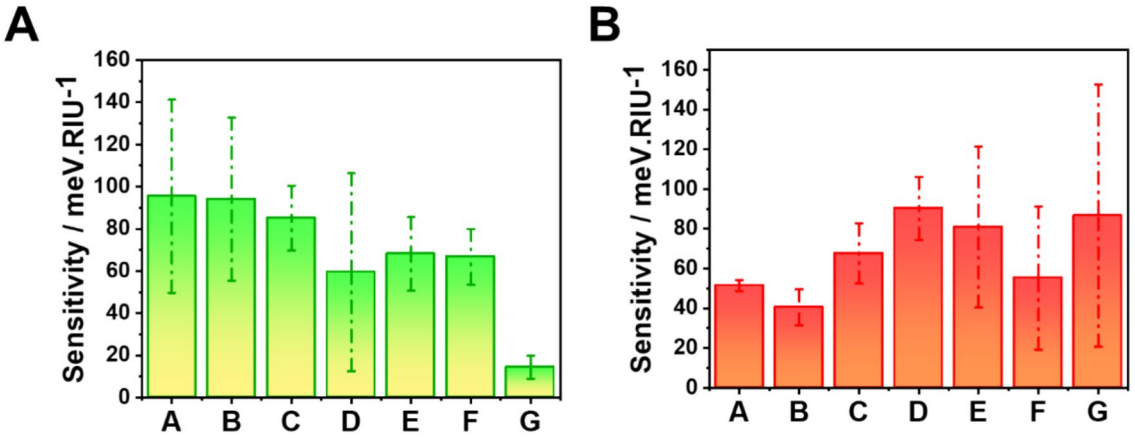

Fig. 6. RI sensitivity of inflection points toward varying local RI media in (**A**) thin AuNRs@Pd_{1mM} and (**B**) thick AuNRs@Pd_{2mM} spectra.

IFs from the second-order derivative on subradiant peak regime showed redshifts for IF G and IF E along with an increase in the local dielectric constant, with values of 2.809 (± 0.027) and 2.476 (± 0.026); 2.807 (± 0.019) and 2.466 (± 0.021); and 2.759 (± 0.017) and 2.431 (± 0.016) eV for air, water, and oil, respectively. The sensitivity of the subradiant peak concavity in thick AuNRs@Pd_{2mM} also demonstrated a higher degree of responsiveness to changes in RI compared to its peak. The surface roughness of plasmonic nanoparticles has been shown to induce broadening of the LSPR peak, thereby reducing its sensitivity to changes in the surrounding dielectric constant of bimetallic nanoparticles[49]. Our previous work has demonstrated that Pd deposition on the Au surface reduces the scattering intensity of bimetallic nanoparticles, as evidenced by the observed decrease in energy in real-time DF microscopy imaging results[18]. Consequently, AuNRs@Pd_{2mM} with thicker shells exhibit lower sensitivity in IFs A-C and IFs E–G compared to AuNRs@Pd_{1mM} with thinner Pd shells.

Similar to the results for thin AuNR@Pd_{1mM}, IF D, which described the Fano dip, showed blueshifts with values of 2.256 (± 0.034); 2.292 (± 0.041); and 2.302 (± 0.033) eV for air, water, and oil, respectively (Fig. 5D). However, the sensitivity of IF D to RI changes in AuNRs@Pd_{2mM} was 1.52 times higher compared to AuNRs@Pd_{1mM}, with the repeatability of IF D in each medium slightly higher than that of the thin AuNRs@Pd_{1mM} (Figs. 6 and S11). A comprehensive comparison of sensitivity between thin AuNRs@Pd_{1mM} and thick AuNRs@Pd_{2mM} across different local RI is presented in Fig. 6. The data reproducibility of each IF point across various refractive indices exhibited relatively good results, proving the reliability of the IF method in determining spectral changes in the multimodal scattering peaks of single AuNRs@Pd (Fig. S11).

Conclusions

In summary, we investigated the LSPR scattering spectra of single AuNRs@Pd with two different Pd shell thicknesses and morphologies. AuNRs@Pd showed characteristic subradiant and superradiant peaks, as well as Fano resonance as a spectral dip. We elucidated the effect of Pd shell thickness on the scattering spectra of these bimetallic nanoparticles. Additionally, we revealed the effect of local RIs on the subradiant and superradiant peak energies, as well as the Fano dip in the scattering spectra of AuNRs@Pd with different Pd shell thicknesses. We demonstrated the applicability of IFs in detecting peak and dip changes across different RIs. Thin AuNRs@Pd_{1mM} displayed a more pronounced sensitivity to peak shifts in response to variations in local RIs compared to thick AuNRs@Pd_{2mM}. In contrast, thick AuNRs@Pd_{2mM} exhibited greater sensitivity to changes in curvature near the subradiant and superradiant peak energies, rather than peak shift sensitivity across different local RIs. Moreover, we observed a more noticeable shift in the Fano dip in thick AuNRs@Pd_{2mM} compared to thin AuNRs@Pd_{1mM} across different local RIs. Therefore, we provided a comprehensive elucidation of the changes in the LSPR spectra of AuNRs@Pd in response to varying local RIs, along with a reliable method for determining the peaks and dip of their single-particle scattering spectra.

Experimental methods

Chemicals and materials

Unless specified otherwise, all chemicals were obtained from commercial suppliers and utilized without further alteration. Hexadecyltrimethylammonium bromide (CTAB, purity > 98%), 5-iodosalicylic acid (technical grade), ascorbic acid (purity > 99%), and palladium (II) chloride (purity > 99.9%) were sourced from Sigma-Aldrich (St. Louis, MO, USA). Hydrogen chloride (HCl, purity > 35%) was obtained from DaeJung Chemicals & Metals Co. (Gyeonggi-do, Republic of Korea). CTAB-capped gold nanorods (AuNRs) were acquired from Nanopartz (Loveland, CO, USA). Highly purified water was employed in the formulation of aqueous solutions for synthesis and analysis purposes.

AuNRs@Pd synthesis

An initial AuNR stock solution (25 μg/mL) was diluted into a 1 mL solution containing CTAB (0.05 M) and 5-iodosalicylic acid (0.01 M). The mixture was gently agitated for 30 s and left undisturbed at room temperature

for 10 h. Afterward, 52 µL of AA (0.1 M), 30 µL of the prepared H_2PdCl_4 (2 mM for thick Pd shell, 1 mM for thin Pd shell), and 16 µL of HCl (0.01 M) were introduced into the solution. The synthesis environment was then maintained at room temperature for 20 h. The resulting nanoparticles were rinsed with distilled water and subsequently centrifuged at 3000 rpm for 30 min and redispersed in water.

Single particle microscopy and spectroscopy

The synthesized AuNRs@Pd were diluted tenfold using distilled water. Subsequently, the diluted AuNRs@Pd solution underwent sonication for 10 min to prevent nanoparticle aggregation. The solution was then deposited onto pre-cleaned slide glass and left to dry. This process ensured that the density of AuNRs@Pd remained at approximately 1.0 μm^{-2} for single-particle characterization. DF microscopy imaging was conducted employing a custom-built setup comprising a Nikon inverted microscope (ECLIPSE Ti-U, Japan) and an electron-multiplying charge-coupled device (EMCCD) camera (iXon Ultra 897, Andor, UK). A system comprised of a Nikon DF condenser and a Nikon Plan Fluor 100×/0.5–1.3 oil iris objective lens were utilized in DF microscopy. Furthermore, DF scattering spectra were obtained using an Andor spectrometer (SHAMROCK 303i, SR-303I-A, UK) coupled with an Andor CCD camera (Newton DU920P-OE, UK). The objective lens was adjusted to optimize the positioning of scattered light of the single-particle using ANDOR software. The scattered light collected by the objective lens was directed to the spectrometer, where it was dispersed by a grating (300 lines/mm) and detected by the CCD camera. DF spectroscopic analysis was done by using microscope camera system at total-period analysis center for Ulsan chemical industry of Korea Basic Science Institute (KBSI).

Data availability

The datasets used during this study available from the corresponding author on reasonable request.

Received: 21 March 2024; Accepted: 26 August 2024
Published online: 30 August 2024

References

1. Li, X. *et al.* Nanomedicine targets endogenous copper ions for disease diagnosis and therapy. *Chem. Eng. J.* **472**, 144951. https://doi.org/10.1016/j.cej.2023.144951 (2023).
2. Fu, Q. *et al.* NIR-II photoacoustic reporter for biopsy-free and real-time assessment of Wilson's disease. *Small* **17**, 2008061. https://doi.org/10.1002/smll.202008061 (2021).
3. Kim, G. W., Lee, S. Y. & Ha, J. W. Three-dimensional defocused orientation sensing of single bimetallic core-shell gold nanorods as multifunctional optical probes. *Analyst* **142**, 899–903. https://doi.org/10.1039/c6an02280d (2017).
4. Su, G. X. *et al.* Controlled deposition of palladium nanodendrites on the tips of gold nanorods and their enhanced catalytic activity. *Nanoscale* **9**, 12494–12502. https://doi.org/10.1039/c7nr04046f (2017).
5. Yoshi, T., Kuwahara, Y., Mori, K. & Yamashita, H. Design of Pd-graphene-Au nanorod nanocomposite catalyst for boosting suzuki-miyaura coupling reaction by assistance of surface plasmon resonance. *J. Phys. Chem. C* **123**, 24575–24583. https://doi.org/10.1021/acs.jpcc.9b06609 (2019).
6. Fan, H. Z. *et al.* Plasmon-enhanced oxidase-like activity and cellular effect of Pd-coated gold nanorods. *ACS Appl. Mater. Inter.* **11**, 45416–45426. https://doi.org/10.1021/acsami.9b16286 (2019).
7. Forcherio, G. T. *et al.* Single-particle insights into plasmonic hot carrier separation augmenting photoelectrochemical ethanol oxidation with photocatalytically synthesized Pd-Au bimetallic nanorods. *ACS Nano* **16**, 12377–12389. https://doi.org/10.1021/acsnano.2c03549 (2022).
8. Mueller, N. S. *et al.* Deep strong light-matter coupling in plasmonic nanoparticle crystals. *Nature* **583**, 780–784. https://doi.org/10.1038/s41586-020-2508-1 (2020).
9. Kermanshahian, K., Yadegar, A., Moghimi, H. & Ghourchian, H. The synergy of Fe_3O_4@Au and molybdate as HRP-mimetic catalysts for gold nanorods etching: Development of an ultrasensitive genosensor for detection of Helicobacter pylori. *Sens. Actuators B Chem.* **371**, 132600. https://doi.org/10.1016/j.snb.2022.132600 (2022).
10. Mahajan, H. *et al.* Well-designed Au nanorod-doped CuO core-shell nanocube-embedded reduced graphene oxide composite for efficient removal of a water pollutant dye. *ACS Omega* **5**, 24799–24810. https://doi.org/10.1021/acsomega.0c03487 (2020).
11. Wei, H. S. *et al.* Supported Au-Ni nano-alloy catalysts for the chemoselective hydrogenation of nitroarenes. *Chin. J. Catal.* **36**, 160–167. https://doi.org/10.1016/S1872-2067(14)60254-0 (2015).
12. Yang, D. R., Chi, C., Ni, M., Sun, Y. B. & Xia, X. H. Superior HER activity of rGO@AuNRs@SAC-Pt promoted by maximized electronic interaction and plasmonic hot carriers. *J. Phys. Chem. C* **126**, 20235–20242. https://doi.org/10.1021/acs.jpcc.2c06424 (2022).
13. Yang, X. B. *et al.* Modulating electronic structure of an Au-nanorod-core-PdPt-alloy-shell catalyst for efficient alcohol electrooxidation. *Adv. Energy Mater.* **11**, 2100812. https://doi.org/10.1002/aenm.202100812 (2021).
14. Khlebtsov, B. N., Burov, A. M. & Khlebtsov, N. G. Polydopamine coating decreases longitudinal plasmon of Au nanorods: Experiment and simulations. *Appl. Mater. Today* **15**, 67–76. https://doi.org/10.1016/j.apmt.2018.12.017 (2019).
15. Ryu, K. R., Kim, G. W. & Ha, J. W. Localized surface plasmon resonance inflection points for improved detection of chemisorption of 1-alkanethiols under total internal reflection scattering microscopy. *Sci. Rep.* **11**, 12902. https://doi.org/10.1038/s41598-021-92410-w (2021).
16. Kahn, A. Fermi level, work function and vacuum level. *Mater. Horiz.* **3**, 7–10. https://doi.org/10.1039/C5MH00160A (2016).
17. Min, K. A., Park, J., Wallace, R. M., Cho, K. & Hong, S. Reduction of Fermi level pinning at Au-MoS2 interfaces by atomic passivation on Au surface. *2D Mater.* **4**, 015019. https://doi.org/10.1088/2053-1583/4/1/015019 (2017).
18. Firmanti, M. I. & Ha, J. W. Elucidating surface plasmon damping and fano resonance induced by epitaxial growth of palladium on single gold nanorods. *J. Phys. Chem. Lett.* **14**, 8016–8023. https://doi.org/10.1021/acs.jpclett.3c02049 (2023).
19. Wang, Q. Y. *et al.* Plasmonic-induced inhibition and enhancement of the electrocatalytic activity of Pd-Au hetero-nanoraspberries for ethanol oxidation. *J. Power. Sources* **316**, 29–36. https://doi.org/10.1016/j.jpowsour.2016.03.057 (2016).
20. Chernyshev, V. M. & Ananikov, V. P. Nickel and palladium catalysis: Stronger demand than ever. *ACS Catal.* **12**, 1180–1200. https://doi.org/10.1021/acscatal.1c04705 (2022).
21. Subaramanian, M., Sivakumar, G. & Balaraman, E. Recent advances in nickel-catalyzed C-C and C-N bond formation via HA and ADC reactions. *Org. Biomol. Chem.* **19**, 4213–4227. https://doi.org/10.1039/d1ob00080b (2021).
22. Titova, Y. Y. & Schmidtb, F. K. Directed design of hydrogenation Ziegler systems. *New J. Chem.* **45**, 4525–4533. https://doi.org/10.1039/d0nj05689h (2021).

23. Zhang, Q. & Guan, J. Atomically dispersed catalysts for hydrogen/oxygen evolution reactions and overall water splitting. *J. Power Sources* **471**, 228446. https://doi.org/10.1016/j.jpowsour.2020.228446 (2020).
24. Hegde, H. R., Chidangil, S. & Sinha, R. K. Refractive index sensitivity of Au nanostructures in solution and on the substrate. *J. Mater. Scix: Mater. El.* **33**, 4011–4024. https://doi.org/10.1007/s10854-021-07593-9 (2022).
25. Zhang, K. J., Lu, D. B., Da, B. & Ding, Z. J. Coupling of surface plasmon modes and refractive index sensitivity of hollow silver nanoprism. *Sci. Rep.* **8**, 15993. https://doi.org/10.1038/s41598-018-34477-6 (2018).
26. Zhu, J., Meng, L.-N., Weng, G.-J., Li, J.-J. & Zhao, J.-W. Improve the plasmonic optical tunability of Au nanorod by Pt coating: The application in refractive index sensing. *Eur. Phy. J. D* **75**, 192. https://doi.org/10.1140/epjd/s10053-021-00195-4 (2021).
27. Hu, J. W. *et al.* Palladium-coated gold nanoparticles with a controlled shell thickness used as surface-enhanced Raman scattering substrate. *J. Phys. Chem. C* **111**, 1105–1112. https://doi.org/10.1021/jp0652906 (2007).
28. Li, Z. D., Wang, R. & Kurouski, D. Nanoscale photocatalytic activity of gold and gold-palladium nanostructures revealed by tip-enhanced Raman spectroscopy. *J. Phys. Chem. Lett.* **11**, 5531–5537. https://doi.org/10.1021/acs.jpclett.0c01631 (2020).
29. Sarina, S. *et al.* Enhancing catalytic performance of palladium in gold and palladium alloy nanoparticles for organic synthesis reactions through visible light irradiation at ambient temperatures. *J. Am. Chem. Soc.* **135**, 5793–5801. https://doi.org/10.1021/ja400527a (2013).
30. Kaiser, J. *et al.* Catalytic activity of nanoalloys from gold and palladium. *Phys. Chem. Chem. Phys.* **14**, 6487–6495. https://doi.org/10.1039/c2cp23974d (2012).
31. Ortiz, N., Hong, S. J., Fonseca, F., Liu, Y. & Wang, G. F. Anisotropic overgrowth of palladium on gold nanorods in the presence of salicylic acid family additives. *J. Phys. Chem. C* **121**, 1876–1883. https://doi.org/10.1021/acs.jpcc.6b12024 (2017).
32. Chen, P. & Liedberg, B. Curvature of the localized surface plasmon resonance peak. *Anal. Chem.* **86**, 7399–7405. https://doi.org/10.1021/ac500883x (2014).
33. Heo, S. E. & Ha, J. W. Improved refractive index sensitivity of localized surface plasmon resonance inflection points in amalgamated gold nanorods with mesoporous silica shell. *Microchem. J.* **181**, 107781. https://doi.org/10.1016/j.microc.2022.107781 (2022).
34. Tsalu, P. V., Kim, G. W., Hong, J. W. & Ha, J. W. Homogeneous localized surface plasmon resonance inflection points for enhanced sensitivity and tracking plasmon damping in single gold bipyramids. *Nanoscale* **10**, 12554–12563. https://doi.org/10.1039/c8nr03311k (2018).
35. Zheng, Z. K., Tachikawa, T. & Majima, T. Plasmon-enhanced formic acid dehydrogenation using anisotropic Pd-Au nanorods studied at the single-particle level. *J. Am. Chem. Soc.* **137**, 948–957. https://doi.org/10.1021/ja511719g (2015).
36. Jing, H. & Wang, H. Controlled overgrowth of Pd on Au nanorods. *Crystengcomm.* **16**, 9469–9477. https://doi.org/10.1039/c4ce00601a (2014).
37. Wang, M., Cao, M., Chen, X. & Gu, N. Subradiant plasmon modes in multilayer metal-dielectric nanoshells. *J. Phys. Chem. C* **115**, 20920–20925. https://doi.org/10.1021/jp205736d (2011).
38. Zhan, Y. H., Lei, D. Y., Li, X. F. & Maier, S. A. Plasmonic Fano resonances in nanohole quadrumers for ultra-sensitive refractive index sensing. *Nanoscale* **6**, 4705–4715. https://doi.org/10.1039/c3nr06024a (2014).
39. Ameri, A. *et al.* Rapid and facile microwave-assisted synthesis of palladium nanoparticles and evaluation of their antioxidant properties and cytotoxic effects against fibroblast-like (HSkMC) and human lung carcinoma (A549) cell lines. *Biol. Trace Elem. Res.* **197**, 132–140. https://doi.org/10.1007/s12011-019-01984-0 (2020).
40. Mallikarjuna, K., Raju, B. D. P., Park, S. & Kim, H. Synthesis and catalytic activity of alkylamine-capped ultra-small palladium nanoparticles for organic pollutant degradation. *J. Clust. Sci.* **28**, 2833–2846. https://doi.org/10.1007/s10876-017-1262-5 (2017).
41. Meva, F. E. *et al.* Silver and palladium nanoparticles produced using a plant extract as reducing agent, stabilized with an ionic liquid: Sizing by X-ray powder diffraction and dynamic light scattering. *J. Mater. Res. Technol.* **8**, 1991–2000. https://doi.org/10.1016/j.jmrt.2018.12.017 (2019).
42. Moumen, A. *et al.* Microwave assisted synthesis of palladium nanoparticles in an aqueous emulsion of copolymer: Application to catalysis. *J. Clust. Sci.* **28**, 2817–2832. https://doi.org/10.1007/s10876-017-1259-0 (2017).
43. Tsuji, M., Uto, K., Hayashi, J. I. & Yoshiwara, A. Synthesis of flower-like AuPd@SiO nanoparticles with a broad light extinction for application to efficient dye-sensitized solar cells. *Part. Part. Syst. Char.* **35**, 1700396. https://doi.org/10.1002/ppsc.201700396 (2018).
44. Paliwal, P., Blech, A., Koch, C. P. & Narevicius, E. Fano interference in quantum resonances from angle-resolved elastic scattering. *Nat. Commun.* **12**, 7249. https://doi.org/10.1038/s41467-021-27556-2 (2021).
45. Vivó-Truyols, G. & Schoenmakers, P. J. Automatic selection of optimal Savitzky-Golay smoothing. *Anal. Chem.* **78**, 4598–4608. https://doi.org/10.1021/ac0600196 (2006).
46. Heo, S. E. & Ha, J. W. Single-particle study: refractive index sensitivity of localized surface plasmon resonance inflection points in mesoporous silica-coated gold nanorods. *Biochip J.* **16**, 183–190. https://doi.org/10.1007/s13206-022-00061-4 (2022).
47. Jeon, H. B., Tsalu, P. V. & Ha, J. W. Shape effect on the refractive index sensitivity at localized surface plasmon resonance inflection points of single gold nanocubes with vertices. *Sci. Rep.* **9**, 13635. https://doi.org/10.1038/s41598-019-50032-3 (2019).
48. Hong, Y. A. & Ha, J. W. Enhanced refractive index sensitivity of localized surface plasmon resonance inflection points in single hollow gold nanospheres with inner cavity. *Sci. Rep.* **12**, 6983. https://doi.org/10.1038/s41598-022-11197-6 (2022).
49. Feng, Z. Q., Jia, Y. & Cui, H. Y. Engineering the surface roughness of the gold nanoparticles for the modulation of LSPR and SERS. *J. Colloid. Interf. Sci.* **672**, 1–11. https://doi.org/10.1016/j.jcis.2024.05.217 (2024).
50. Sun, L. C. *et al.* Multifaceted gold-palladium bimetallic nanorods and their geometric, compositional, and catalytic tunabilities. *ACS Nano* **11**, 3213–3228. https://doi.org/10.1021/acsnano.7b00264 (2017).

Acknowledgements

This work was supported by the National Research Foundation of Korea (NRF) funded by the Korean government (MSIP) (Nos. RS-2023-00208346 and 2019R1A6A1A11053838).

Author contributions

M.I.F performed the single-particle scattering measurements. M.I.F and J.W.H. analyzed the data and wrote the paper.

Competing interests

The authors declare no competing interests.

Additional information

Supplementary Information The online version contains supplementary material available at https://doi.org/10.1038/s41598-024-71141-8.

Correspondence and requests for materials should be addressed to J.W.H.